electronic materials

MDPI

Article

Low-Temperature Oxygen Sensing Performance and Oxygen Ion Irradiation Response of 8YSZ-Based Sensors in Liquid Lead-Bismuth Eutectic

Ziyue Mao, Yu Wang, Zhengze Xiang, Ruixian Liang * and Fenglei Niu

School of Nuclear Science and Engineering, North China Electric Power University, Beijing 102206, China
* Correspondence: lrx@ncepu.edu.cn

Abstract

Dissolved oxygen concentration is a key parameter determining the oxidation and corrosion behavior of structural materials in lead-based fast reactor coolants. Therefore, achieving high-precision in-situ oxygen measurement in LBE systems is a fundamental technical requirement for implementing oxygen-controlled corrosion protection. Currently, nuclear-grade Bi/Bi_2O_3 solid-state electrochemical oxygen sensors have a minimum effective operating temperature of 350 °C, which prevents them from meeting the real-time oxygen monitoring needs under low-temperature conditions. This temperature limitation has become a major bottleneck for the engineering application of oxygen control technology. To address these requirements and challenges, this study develops a novel electrochemical oxygen sensor based on an 8 mol% Y_2O_3-stabilized ZrO_2 (8YSZ) solid electrolyte and $La_{0.6}Sr_{0.4}Co_{0.2}Fe_{0.8}O_{3\pm\delta}$ (LSCF) electrode system. Comparative experiments with Bi/Bi_2O_3 sensors are conducted to quantitatively assess the advantages of the LSCF/Air sensor in low-temperature applications within 205~550 °C. Furthermore, considering the irradiation environment in nuclear reactors, oxygen ion irradiation was employed as an accelerated simulation method to preliminarily investigate the electrochemical transport properties of 8YSZ after irradiation. The effects of oxygen ion irradiation on the apparent impedance and apparent oxygen ion conductivity of 8YSZ were evaluated. The results show that the LSCF/Air oxygen sensor has the potential to extend the lower operating-temperature limit of 8YSZ-based oxygen sensors in static, oxygen-saturated LBE environments. Oxygen ion irradiation increased the apparent impedance and decreased the apparent ionic conductivity of the tested 8YSZ samples. These results provide preliminary experimental data for the development of oxygen sensors for oxygen monitoring and corrosion control in liquid-metal-cooled reactor systems over a wider temperature range.

Keywords: liquid lead-bismuth eutectic alloy (LBE); oxygen sensors; 8YSZ; ion irradiation

Check for updates

Academic Editor: Lijia Liu

Received: 14 July 2026
Revised: 14 August 2026
Accepted: 24 August 2026
Published: 1 September 2026

Copyright: © 2026 by the authors. Licensee MDPI, Basel, Switzerland. This article is an open access article distributed under the terms and conditions of the Creative Commons Attribution (CC BY) license.

1. Introduction

The Lead-Bismuth Fast Reactor (LFR) is one of the six candidate reactor designs for Generation IV nuclear systems, offering a combination of advantages including high uranium resource utilization, strong transmutation capability for actinides, low production of long-lived radioactive waste, and outstanding inherent safety. However, under the harsh operating conditions of high temperature, intense irradiation, and dynamic thermo-hydraulic coupling, liquid LBE exhibits significant synergistic effects of chemical corrosion and dissolution erosion on structural materials such as austenitic and ferritic/martensitic

steels, posing a critical technical bottleneck that restricts the long-term safe operation of reactors. Engineering experience from Russia with LBE-cooled reactors like Alpha-class nuclear submarines demonstrates that dissolved oxygen concentration is one of the most crucial parameters governing the thermochemical behavior of LBE coolant [1]. In the liquid LBE system, dissolved oxygen not only directly participates in redox reactions at the interface between coolant and structural materials, but also acts as a kinetic controlling factor in the nucleation, growth, and evolution of oxide films, dominating the phase composition, density, and interfacial adhesion strength of protective oxides such as Fe_3O_4 and $(Fe, Cr)_3O_4$. When dissolved oxygen concentration is maintained within reasonable range (10^{-8}~10^{-6}wt.%), a continuous, dense, and self-healing dual-layer oxide film can form in situ on steel surfaces, effectively suppressing the continuous dissolution and mass transfer of base metal elements (Fe, Cr, Ni) [2]. Conversely, if oxygen concentration deviates from this optimal window—excessively high levels triggering over-oxidation and spallation, while excessively low levels result in incomplete or locally exposed passive films—serious safety incidents such as pitting corrosion, intergranular corrosion, flow-accelerated corrosion, and even coolant circuit blockage may occur. Therefore, developing in-situ monitoring technologies for dissolved oxygen that are linear, highly accurate, fast-responsive, and long-term stable has become a prerequisite and core challenge for ensuring the safe and reliable operation of LBE cooling systems.

Yttria-stabilized zirconia (YSZ), a representative zirconia-based oxygen ion-conducting ceramic, is widely recognized as the most mature and engineering-feasible solid electrolyte material system for high-temperature electrochemical oxygen sensors due to its excellent oxygen ion conductivity, good chemical inertness (especially toward molten LBE), superior mechanical stability, and potential resistance to radiation degradation. By establishing a stable oxygen concentration difference electromotive force, it enables thermodynamic quantification of oxygen activity in LBE, providing real-time and reliable sensing support for closed-loop oxygen control strategies. Given the decisive influence of oxygen activity on the corrosion rate of structural materials in LBE coolant, oxide film evolution pathways, and the service lifetime of coolant circuits, YSZ-based solid-state electrochemical oxygen sensors have been designated as essential enabling sensor components in advanced international nuclear research programs such as EUROTRANS [3], ALFRED [4], and BREST-OD-300 [5] for liquid-metal-cooled fast reactors.

Currently, the Bi/Bi_2O_3 reference-type oxygen sensor is the most extensively studied and engineering-validated electrochemical oxygen measurement solution for liquid LBE. Askhadullin et al. [6,7] employed Al_2O_3-doped YSZ as a solid electrolyte, demonstrating that this modification significantly lowers the sintering temperature of YSZ while enhancing its thermal shock resistance and mechanical strength. Although they suggested potential applicability in irradiation environments, critical experimental data on irradiation dose, energy spectrum, and material performance degradation were not provided, leaving the oxygen ion transport stability of YSZ ceramics under actual reactor irradiation conditions without empirical support. The Bi/Bi_2O_3–YSZ sensor developed by Courouau et al. [8] exhibited good repeatability, low time drift, reasonable response speed, and structural robustness within a static LBE environment at temperatures between 280~550 °C; however, its measurement uncertainty was as high as ±40%. Subsequent dynamic testing in the STELLA loop further revealed systematic zero-point offsets ranging from several to tens of millivolts across all sensors, with significant accuracy degradation below 370 °C. More notably, after 1400 h of continuous operation, cracking occurred in the YSZ ceramic tube, indicating potential long-term thermomechanical reliability issues [9]. Schroer et al. [10] utilized Bi/Bi_2O_3 reference electrode paired with YPSZ (yttria-partially stabilized zirconia) electrolyte, achieving ceramic-to-metal bonding via mechanical sealing. After calibration,

the electromotive force (EMF) deviation was maintained within ±5 mV over 350~700 °C; however, thermal cycling frequently induced cracking in the Bi/Bi_2O_3 electrode, exposing shortcomings in interface stability. Lim et al. [11] developed a sensor based on Bi/Bi_2O_3 and 5YSZ, finding that even with high-input-impedance (>10 GΩ) signal acquisition circuit, the EMF showed significant nonlinear deviations when operating temperature dropped to 200 °C. Bassini et al. [12] reported that an 8YSZ-based Bi/Bi_2O_3 sensor could operate down to 290 °C, slightly above the melting point of Bi, but did not validate its response dynamics or long-term stability at lower temperatures. Studies by Wu et al. [13] and Kurata et al. [14] consistently indicated that the EMF of Bi/Bi_2O_3 sensors only closely follows Nernstian behavior at temperatures $\geq$ 360 °C or within the 350~500 °C range; below this threshold, the readings severely deviate from theoretical values, and all models require on-site calibration to produce usable data.

Bi/Bi_2O_3 sensors have been validated in experimental lead-based reactor environments and demonstrate engineering applicability. However, their lower measurement temperature limit is typically restricted to around 350 °C, and the degradation mechanisms under irradiation conditions remain unclear. Ion irradiation is often used as an accelerated method to investigate selected irradiation-damage effects in YSZ. However, ion irradiation cannot completely reproduce the damage characteristics of neutron irradiation because of differences in penetration depth, damage distribution, implanted species, and defect-generation mechanisms. Zhu et al. [15] irradiated 4~6 mol% YSZ with heavy ions and observed irradiation-induced phase transformation and void formation, with 6YSZ exhibiting the largest void sizes. Ghyngazov et al. [16] reported that argon ion beam irradiation could induce surface phase transformation in 3YSZ, while other studies showed that ion irradiation may also affect oxygen ion conductivity in the irradiated region [17]. Pu et al. [18] exposed 8YSZ to helium ion irradiation and observed phase evolution, irradiation hardening, and changes in mechanical properties at sufficiently high fluences. Helium bubbles and dislocation structures were also reported. Alin et al. [19] demonstrated that YSZ containing a high tetragonal-phase fraction underwent irradiation-induced transformation toward the cubic phase after xenon-ion irradiation, accompanied by lattice deformation and lattice expansion. Collectively, these studies indicate that ion irradiation can induce microstructural changes in YSZ, including point defects, defect clusters, phase transformation, lattice distortion, bubble formation, swelling, and hardening. These changes may affect the mechanical and electrochemical properties of YSZ. However, the specific effects depend strongly on the initial YSZ composition and phase structure, ion species, irradiation energy, fluence, damage level, irradiation temperature, and post-irradiation test conditions. Therefore, the relationship between irradiation-induced microstructural changes and oxygen ion transport requires further systematic investigation.

To address the aforementioned technical limitations, this study aims to develop a novel air-reference oxygen sensor based on LSCF (lanthanum strontium cobalt ferrite), a mixed-conducting material. LSCF exhibits excellent mixed ionic–electronic conductivity and outstanding electrochemical catalytic activity, enabling sustained oxygen reduction reaction rates across moderate to low temperature ranges. This capability holds promise for fundamentally overcoming the temperature limitations of Bi/Bi_2O_3 sensors, extending reliable measurement down to 205 °C or even lower. Furthermore, this research systematically investigates the evolution of electrochemical properties in 8YSZ electrolyte following oxygen ion irradiation, aiming to phenomenologically evaluate the apparent degradation of ionic transport performance under specific accelerated ion damage. By integrating material optimization with irradiation evaluation, this work seeks to provide a promising prototype sensing solution for oxygen control in liquid LBE coolants that demonstrates low-temperature adaptability and preliminary irradiation response.

2. Fundamental Theory of Electrochemical Oxygen Sensors

The sensing function of an oxygen sensor originates from the electromotive-force response of a solid-electrolyte electrochemical cell. Its basic operating principle is as follows: the solid electrolyte mainly conducts oxygen ions. When there is a difference in oxygen activity between its two sides, an electrochemical-potential difference is established across the solid electrolyte. This electrochemical process establishes a potential difference, or EMF, between the two electrodes. By accurately measuring this EMF value and applying the Nernst equation, the oxygen activity or equilibrium oxygen partial pressure in the measured medium can be determined. The working principle of the oxygen sensor is shown in Figure 1.

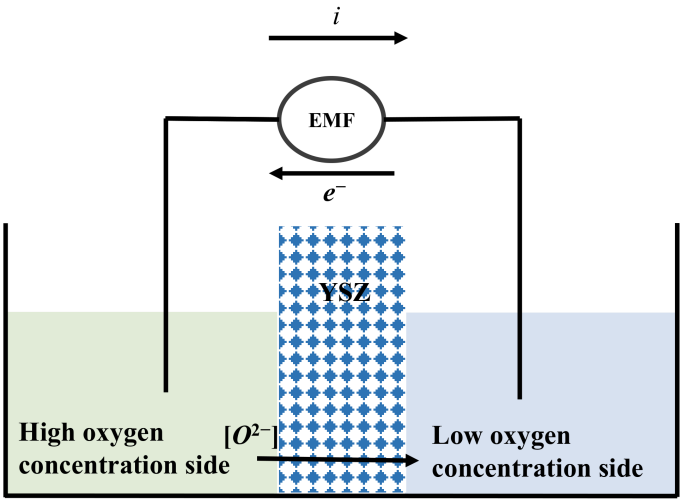


Figure 1. Schematic diagram of the working principle of the oxygen sensor.

The theoretical output EMF of the oxygen sensor can be expressed using the Nernst equation in terms of the equilibrium oxygen partial pressures, as shown in the following equation.

$$E_{th} = \frac{RT}{4F} \ln \frac{P_{O_2,ref}}{P_{O_2,LBE}} \quad (1)$$

The theoretical electromotive force of the oxygen sensor, E_{th}, can be expressed in Volts (V). The gas constant, denoted R, is defined as 8.31441 J/(K·mol). T is the absolute temperature in Kelvin (K). It is evident that Faraday's constant, denoted by F, is precisely 96,484.6 C/mol. $P_{O_2,ref}$ is defined as the partial pressure of oxygen on the side of the reference electrode. The term $P_{O_2,LBE}$ is used to denote the partial pressure of dissolved oxygen in LBE. In the context of air reference oxygen sensors, the partial pressure of oxygen on the reference electrode side is equivalent to the partial pressure of oxygen in the atmosphere, which is measured at 0.209. In the context of metal/metal oxide reference oxygen sensors, the oxygen partial pressure at the reference electrode side is determined by the redox equilibrium of the following general chemical reaction, which is expressed at constant temperature. The following equation is applicable to a reaction that consumes 1 mol of oxygen.

$$\frac{2x}{y}M + O_2 = \frac{2}{y}M_xO_y \quad (2)$$

The metal (M)/metal oxide (M_xO_y) reference is defined by the stoichiometric coefficients of the metal (x) and oxygen (y).

The unit of free enthalpy (ΔG^O_{ref}) of production corresponding to the consumption of 1 mol of oxygen is expressed in J/mol. It is imperative to establish the reference side to ensure a constant partial pressure of oxygen. In order to establish thermodynamic

equilibrium of the reaction, the metal and its oxides must be present in excess. The partial pressure of oxygen on the reference side is defined by the following equation.

$$\ln P_{O_2,ref} = \frac{\Delta G^O_{ref}}{RT} \tag{3}$$

It is important to note that PbO is the most stable oxide in LBE, and thus the partial pressure of oxygen in LBE is given by the thermodynamic equilibrium equation for the generation of PbO.

$$2Pb + O_2 \Leftrightarrow 2PbO_{(dissolved)} \tag{4}$$

The lead oxide activity, denoted by a_{PbO}, in liquid LBE systems is determined by the oxygen activity, denoted by a_O. The oxygen activity is defined as shown in the following equation.

$$a_O = \frac{C_O}{C_O^{sat}} \tag{5}$$

C_O is the LBE oxygen concentration in wt.%, and C_O^{sat} is the saturated oxygen concentration of LBE in wt.%. The reaction activity product for the formation of lead oxide in LBE is shown in the following equation.

$$\Delta G^O_{PbO} = -RT \ln \frac{a^2_{PbO}}{a^2_{Pb} P_{O_2,LBE}} \tag{6}$$

The partial pressure of oxygen in LBE is subsequently demonstrated in the ensuing equation.

$$\ln P_{O_2,LBE} = \frac{\Delta G^O_{PbO}}{RT} + 2 \ln \frac{a_O}{a_{Pb}} \tag{7}$$

The saturated oxygen concentration in LBE is shown in the following equation.

$$\ln C_O^{sat} = 7.09 - \frac{10922}{T_{(K)}} \tag{8}$$

The following equation is obtained from the available literature for lead activity (a_{Pb}) in LBE [20]

$$\ln a_{Pb} = -0.8598 - \frac{135.21}{T_{(K)}} \tag{9}$$

The free enthalpies of formation of the various oxides are expressed by the following relations, assuming that all relations are for the consumption of 1 mole of O_2.

$$\Delta G^O_{(J/mol)} = \Delta H^O - \Delta S^O T_{(K)} \tag{10}$$

The present study focuses on the evaluation of the performance of LSCF/Air and Bi/Bi_2O_3 reference sensor. The electrochemical equilibrium equations for different oxygen sensors are shown below.

$$Air, LSCF|YSZ|LBE, PbO \tag{11}$$

$$Bi, Bi_2O_3|YSZ|LBE, PbO \tag{12}$$

The theoretical output EMF of the oxygen sensor is the Nernst equation, and the Nernst equation incorporating Gibbs free energy is expressed as follows:

$$E_{th} = \frac{\Delta H^O_{ref} - \Delta H^O_{PbO}}{4F} - \frac{\Delta S^O_{ref} - \Delta S^O_{PbO}}{4F} T - \frac{RT}{2F} \left(\ln \frac{C_O}{C_O^{SAT}} - \ln a_{Pb} \right) \tag{13}$$

The standard enthalpy and entropy related to the Gibbs free energy of the reaction between bismuth and oxygen can be referenced using the following equations within the temperature range of 400~1000 K [20].

$$\Delta G^{O} = -389.14 + 192.6T \tag{14}$$

As shown above, when the dissolved oxygen in LBE reaches saturation, the output electromotive force of the oxygen sensor depends solely on temperature. The relationship between the output electromotive force and temperature for the LSCF and Bi/Bi_2O_3 electrode oxygen sensor is as follows.

$$LSCF/Air : E_{Air}^{sat} = 1.1281 - 5.86 \times 10^{-4}T \tag{15}$$

$$Bi/Bi_2O_3 : E_{Bi/Bi_2O_3}^{sat} = 0.11976 - 5.39 \times 10^{-5}T \tag{16}$$

3. Experimental Platform

The oxygen-sensor performance-testing platform used in this study is shown in Figure 2. It mainly consists of an LBE vessel, oxygen sensors, thermocouples, a temperature controller, and a signal-acquisition instrument. The main body of the LBE vessel is made of 316L stainless steel, with a 2.5 kW heater mounted on the outer wall to provide heating. A thermal-insulation layer is applied to the outer surface to minimize heat loss and improve the thermal stability of the experimental system. Multiple mounting ports are provided on the sealing flange for installing components such as the oxygen sensors, pressure gauge, and thermocouples. The data-acquisition system employs an Agilent 34980A data-acquisition unit, which provides an input impedance greater than 10 GΩ per channel, thereby reducing the influence of the acquisition system on the high-impedance voltage signals of the oxygen sensors.

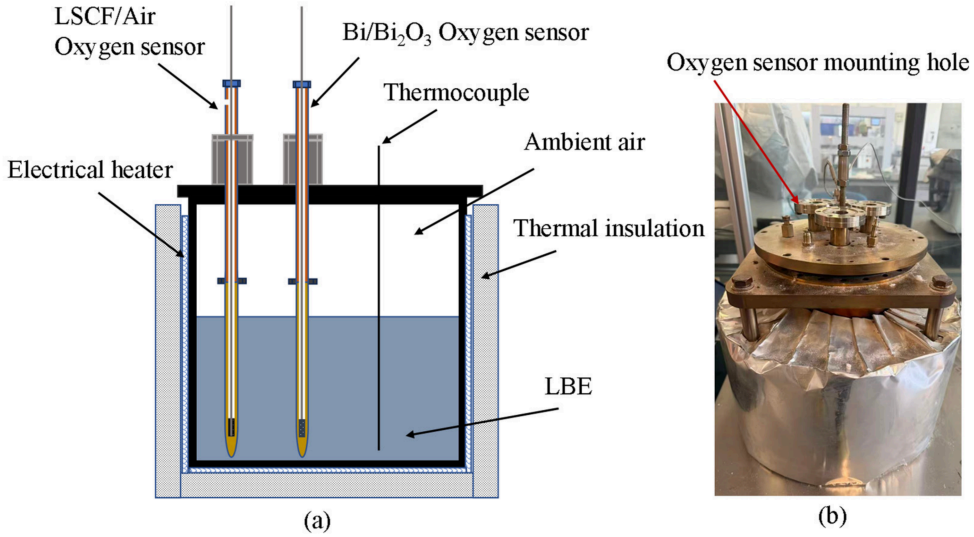


Figure 2. Experimental platform for testing oxygen sensors in LBE: (**a**) schematic diagram of the oxygen-sensor testing system; (**b**) LBE vessel used in the experiments.

The structure of the oxygen sensor mainly consists of an installation flange, a stainless steel support tube, a solid electrolyte ceramic probe, reference electrode material, signal wires, BNC connectors, and sealing components, as shown in Figure 3. The solid-electrolyte ceramic probe serves as the core sensing element of the sensor, fabricated from 8 mol% yttria-stabilized zirconia (8YSZ) as a ceramic tube with one end closed and the other end open. The tube is approximately 150 mm in length, with inner and outer diameters

of 4 mm and 6 mm, respectively. The reference-electrode materials are LSCF (>99.5%, $La_{0.6}Sr_{0.4}Co_{0.2}Fe_{0.8}O_{3\pm\delta}$) and Bi/Bi_2O_3 (>99.9% and >99%, respectively). For the LSCF/Air sensor, LSCF catalyzes oxygen adsorption, dissociation, charge transfer, and oxygen ion incorporation at the LSCF/8YSZ interface. Ambient air provides a reference atmosphere with a nominal oxygen partial pressure of 0.209 atm. By measuring the potential difference between this reference electrode and the outer electrode in contact with LBE, the oxygen activity in the LBE can be determined. Meanwhile, the Bi/Bi_2O_3 system functions as a metal/metal-oxide pair that maintains a thermodynamically defined equilibrium oxygen activity. The coexistence of Bi and Bi/Bi_2O_3 provides a stable reference potential for oxygen-activity measurement. The signal electrode wire is made of high-temperature-resistant 316L stainless steel wire, responsible for transmitting the EMF generated across the 8YSZ ceramic probe to external data-acquisition equipment. The stainless-steel support tube provides mechanical protection and positioning for the internal components. It is made of the same nominal material as the LBE vessel, 316L stainless steel, to reduce additional thermoelectric-potential contributions caused by dissimilar materials in the high-temperature liquid-metal environment.

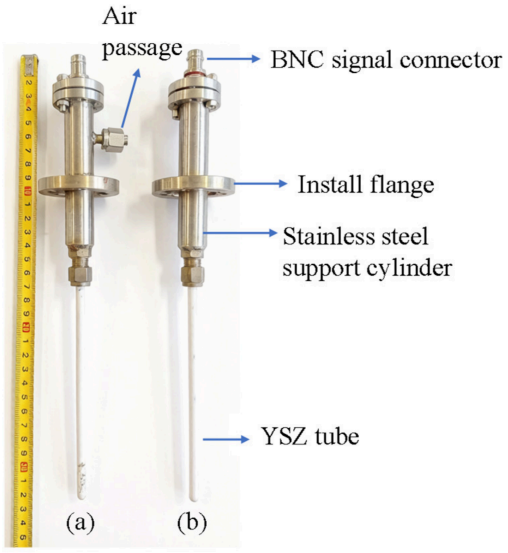


Figure 3. Structures of oxygen sensors with different reference-electrode systems: (**a**) LSCF/Air reference oxygen sensor; (**b**) Bi/Bi_2O_3 reference oxygen sensor.

4. Test Results of Oxygen Sensor

4.1. Analysis of the Electromotive Force Characteristics of Oxygen Sensors

Stepwise cooling tests were conducted separately on the Bi/Bi_2O_3 and LSCF oxygen sensors in saturated oxygen LBE, with results shown in Figure 4. For the Bi/Bi_2O_3 sensor test conditions, the temperature change rate of the LBE was set at 0.3 °C/min, and a target dwell time of 18 h was maintained to ensure full thermal equilibrium at each temperature point, as illustrated in Figure 4a. Overall, the output electromotive force (EMF) of the bismuth-based oxygen sensor closely matched theoretical values, and its temperature-dependent behavior conformed well to the Nernst theory. However, during the initial phase of cooling from the constant-temperature stage, the EMF of the bismuth sensor first decreased and then increased. A distinct signal relaxation phenomenon occurred at the beginning of cooling at each target temperature. This is typically attributed to the combined effects of non-steady-state temperature changes and delayed dynamic responses at the electrode interface. In the early cooling phase, the EMF rapidly declined with decreasing temperature, primarily due to the direct reduction effect of the RT/nF term in

the Nernst equation. However, the subsequent EMF recovery cannot be fully explained by thermodynamics alone; instead, it reflects the interface dynamic response lag under non-steady-state temperature conditions. Specifically, when the temperature decreases, a gradient in oxygen activity develops between the bulk LBE and the electrode interface due to diffusion limitations. Meanwhile, the equilibrium reconstruction of the Bi/Bi_2O_3 reaction at the reference electrode side involves a relaxation process. These two factors together cause the effective interfacial oxygen partial pressure to initially remain low before gradually recovering toward the equilibrium state corresponding to the given temperature, resulting in an observed EMF rebound. This phenomenon indicates that during dynamic cooling, the output of the bismuth oxygen sensor does not uniquely correspond to the thermodynamic equilibrium potential at any given temperature, and reliable readings can only be obtained after the interface relaxation has completed. Once the LBE temperature reaches and stabilizes at the target value, the oxygen sensor's output EMF also gradually stabilizes. Within the temperature range of 550~350 °C, the Bi/Bi_2O_3 oxygen sensor achieved stable signal readings after a 10-h stabilization period. When the temperature decreased from 350 °C toward the target value, the output EMF of the bismuth sensor continued to decrease without recovery, and the signal did not rise—its reading clearly deviated from Nernstian behavior. At the final constant temperature of 295 °C, the output EMF of the bismuth sensor was 35 mV lower than the theoretical value, with significant fluctuations in readings, leading to signal failure.

Unlike the Bi/Bi_2O_3 oxygen sensor, the relaxation phenomenon in the LSCF/Air oxygen sensor is not significant. During stepwise cooling from 550 °C to 250 °C, no noticeable relaxation behavior was observed, indicating that the LSCF/Air material exhibits good response stability and rapid equilibration capability within the medium-to-high temperature range. However, during the initial stage of cooling the LBE temperature from 250 °C toward the target value of 205 °C, a distinct relaxation behavior was observed in the sensor's output electromotive force, as shown in Figure 4b. This suggests that although the LSCF/Air oxygen sensor demonstrates excellent dynamic response characteristics at higher temperatures, its electrochemical equilibrium process is significantly affected at low temperatures—particularly near 205 °C. Possible reasons include a substantial decrease in oxygen ion migration rate within the solid electrolyte at low temperatures, slower kinetics of interfacial charge transfer reactions, and delayed establishment of oxygen partial pressure at the electrode/electrolyte interface, all of which collectively cause the sensor's output electromotive force to require a longer time to reach steady state. This relaxation behavior is especially pronounced during the initial cooling phase, further indicating enhanced sensitivity of the LSCF/Air oxygen sensor to temperature changes under low-temperature conditions. When held at the lowest temperature for up to 20 h, the output voltage of the LSCF/Air oxygen sensor was 10 mV lower than the theoretical value.

Overall, the LSCF/Air oxygen sensor exhibits good accuracy and stability within the temperature range of 205~550 °C, with a maximum relative error of −1.28% between its output electromotive force and the theoretical value, occurring at the lowest temperature. In contrast, the Bi/Bi_2O_3 oxygen sensor shows better accuracy and stability in the range of 350~550 °C; however, when the temperature drops below 350 °C, its output signal deviates from the Nernst behavior, reaching a relative deviation of −39.95% at 295 °C, as shown specifically in Figure 4c.

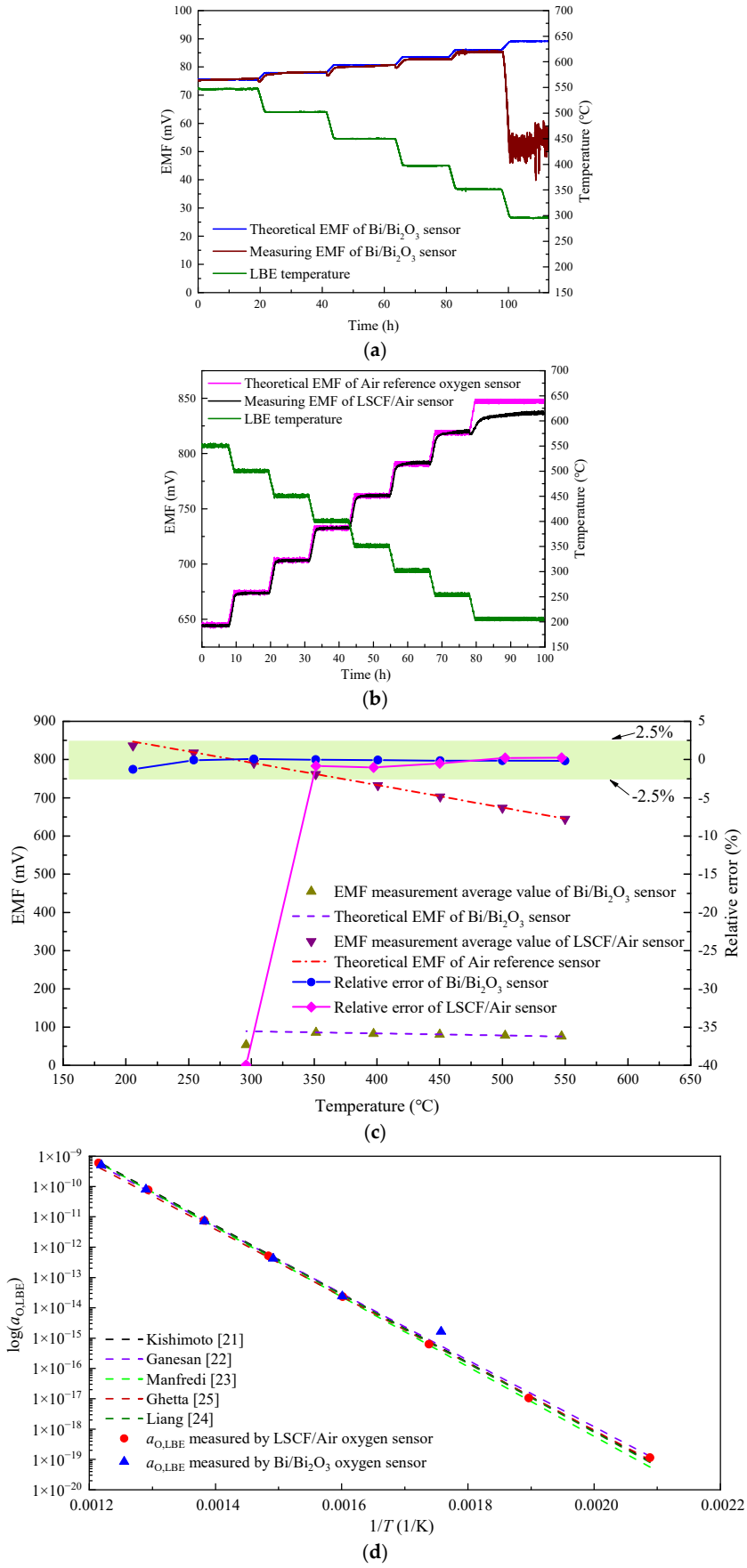


Figure 4. Oxygen measurement results of Bi/Bi_2O_3 and LSCF/Air oxygen sensors during stepwise cooling in LBE; (**a**) Stepwise cooling test results of the Bi/Bi_2O_3 oxygen sensor in the temperature range

of 550~295 °C, (**b**) Stepwise cooling test results of the LSCF/Air oxygen sensor in the temperature range of 550~205 °C, (**c**) Output data analysis of Bi/Bi_2O_3 and LSCF/Air oxygen sensors during the holding stage, (**d**) Oxygen activity measurement results from Bi/Bi_2O_3 and LSCF/Air oxygen sensors.

The oxygen activity data measured by the Bi/Bi_2O_3 and LSCF/Air oxygen sensors are shown in Figure 4d. For the Bi/Bi_2O_3 oxygen sensor, the measured oxygen activity values at temperatures above 295 °C generally fall within the range reported in the literature. Within the operating temperature range of 350~550 °C, the measured oxygen activity in this study showed relative errors ranging from −14.2% to −11.2% compared to the data of Kishimoto et al. [21]. In comparison with Ganesan et al.'s data [22], the maximum relative error was −17.6%, while the minimum was as low as 4.1%. Compared to the data from Manfredi et al. [23], the relative error range is only from −0.83% to +7.2%. Compared to our previous research results [24], the relative errors remained stable within −9.2% to −7.5%. Notably, except for the data of Ghetta et al., the maximum relative errors in all other comparisons occurred at 350 °C; whereas the deviations from Ghetta et al.'s [25] data were most scattered—the largest relative error (+32.5%) occurred at 550 °C, while the smallest (+2.8%) was observed at 350 °C. The oxygen activity data measured by the LSCF/Air oxygen sensor showed relative errors of −7.2% to +31.2% compared to Kishimoto et al.'s results [21], −35.2% to +15.8% compared to Ganesan et al.'s results [22], and the largest deviation—ranging from −0.8% to +106%—compared to Manfredi et al.'s data [23], with the maximum positive deviation occurring at the lowest test temperature (205 °C). Compared to Ghetta et al.'s data [25], the relative error ranged from −16.5% to +38.8%. Except for the data point at 205 °C, the relative error remained stable between −13.7% and −3.4% when compared to our team's previous research results [24].

These differences may arise from variations in experimental conditions, such as differences in the composition of LBE, oxygen-activity definitions, thermodynamic data, temperature measurement, YSZ properties, electrode configurations, and experimental procedures used by different research groups. Therefore, the differences between the present results and the literature data should not be directly treated as the absolute measurement errors of the sensors. Calibration under the actual operating conditions is still required before quantitative oxygen-concentration measurements are performed.

4.2. Electrochemical Performance Analysis of Bi/Bi_2O_3 and LSCF/Air Oxygen Sensors

In this experiment, electrochemical impedance spectroscopy (EIS) measurements were performed using a CHI660E electrochemical workstation for both Bi/$Bi_2O_3$and LSCF/Air oxygen sensors. The purpose was to investigate the interfacial polarization characteristics of solid-state oxygen sensors in a liquid LBE environment. The EIS measurements were conducted under open-circuit potential (OCP) conditions with an AC perturbation amplitude of 10 mV over a frequency range from 10^5 Hz down to 10^{-2} Hz. Prior to each EIS acquisition, the system was stabilized at the target temperature to ensure a steady electrochemical state. The impedance spectra were quantitatively evaluated using ZView2.9c software (or the built-in CHI software) via a complex nonlinear least squares (CNLS) fitting method. Both sensors used an 8YSZ ceramic tube as the solid electrolyte, and the reference electrode material was filled into the inner cavity of the ceramic tube. Because the two oxygen sensors have similar physical mechanisms in charge transfer and mass transport, the equivalent circuit model shown in Figure 5 was used for fitting and analysis. In this model, R_1 represents the ohmic resistance of the system, which is mainly determined by the bulk ionic transport resistance of the 8YSZ solid electrolyte. R_2 is the high-frequency polarization resistance, which characterizes the charge-transfer impedance at the triple-phase boundary (TPB). R_3 is the low-frequency polarization resistance, which reflects the impedance related to oxygen adsorption, dissociation, and diffusion/mass transport inside

the porous electrode. The total polarization resistance, R_p, is defined as the sum of R_2 and R_3.

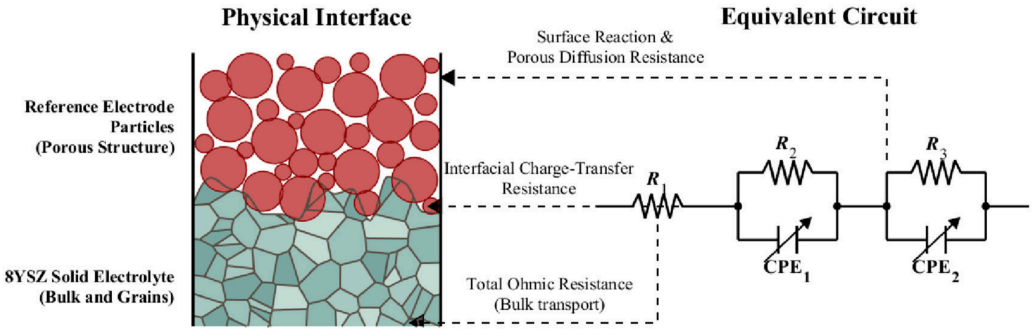


Figure 5. Schematic of the physical electrode–electrolyte interface and the corresponding equivalent circuit model used for fitting the impedance spectra. Component assignments: R_1 (total ohmic resistance), R_2 and CPE_1 (interfacial charge-transfer resistance), R_3 and CPE_2 (surface reaction and porous diffusion resistance).

The fitted Nyquist plots of the LSCF/Air oxygen sensor are shown in Figure 6. At 400 °C, as shown in Figure 6a, the impedance spectrum shows a clear two-capacitive-arc feature, indicating that the oxygen reduction reaction is controlled by multiple elementary steps. The interfacial ion-transfer resistance corresponding to the high-frequency arc is approximately 3717–4774 Ω, while the surface reaction/adsorption-dissociation resistance corresponding to the low-frequency arc is approximately 1152–1185 Ω. The peak imaginary impedance reaches about 1500 Ω.

As the temperature increases, the polarization resistance in each frequency region and the peak imaginary impedance decrease significantly. At 500 °C, as shown in Figure 6c, the total polarization resistance decreases from about 6700 Ω to about 1200 Ω, and the peak imaginary impedance decreases to about 400 Ω. At 600 °C, as shown in Figure 6e, the impedance arcs further shrink. This trend indicates that increasing temperature effectively accelerates the oxygen exchange kinetics on the LSCF electrode surface and the interfacial oxygen ion injection process. As a result, the polarization impedance at the electrode/electrolyte interface is significantly reduced. This is consistent with the enhanced mixed conductivity and surface catalytic activity of LSCF at high temperature.

The Bode phase-angle plots of the LSCF/Air oxygen sensor, shown in Figure 6b,d,f, exhibit broad frequency-distribution characteristics in the temperature range of 400–600 °C. The response covers a wide frequency range from low to high frequencies. This indicates that the oxygen reduction reaction involves multiple elementary steps with different relaxation times. These steps can be distinguished in the frequency spectrum. The low-frequency region corresponds to the diffusion of gaseous oxygen in the porous LSCF electrode and its mass transport to the active reaction sites. The medium-frequency region reflects the adsorption and dissociation of oxygen molecules on the LSCF electrode surface. The high-frequency region represents the interfacial transfer of oxygen ions from the LSCF electrode to the 8YSZ electrolyte.

As the temperature increases, the phase-angle peak generally shifts toward lower frequencies. This phenomenon can be attributed to the mixed ionic–electronic conducting nature of LSCF. At high temperature, the electrochemically active region of LSCF expands from the traditional triple-phase boundary to the whole exposed electrode surface, which significantly increases the electrochemically active area and interfacial capacitance. According to the relaxation–time relationship, the increase in capacitance leads to an increase in the system time constant, which appears as a shift in the phase-angle peak toward lower

frequencies. This evolution also indirectly confirms that increasing temperature enhances the mixed oxygen ion/electron transport ability in the LSCF bulk.

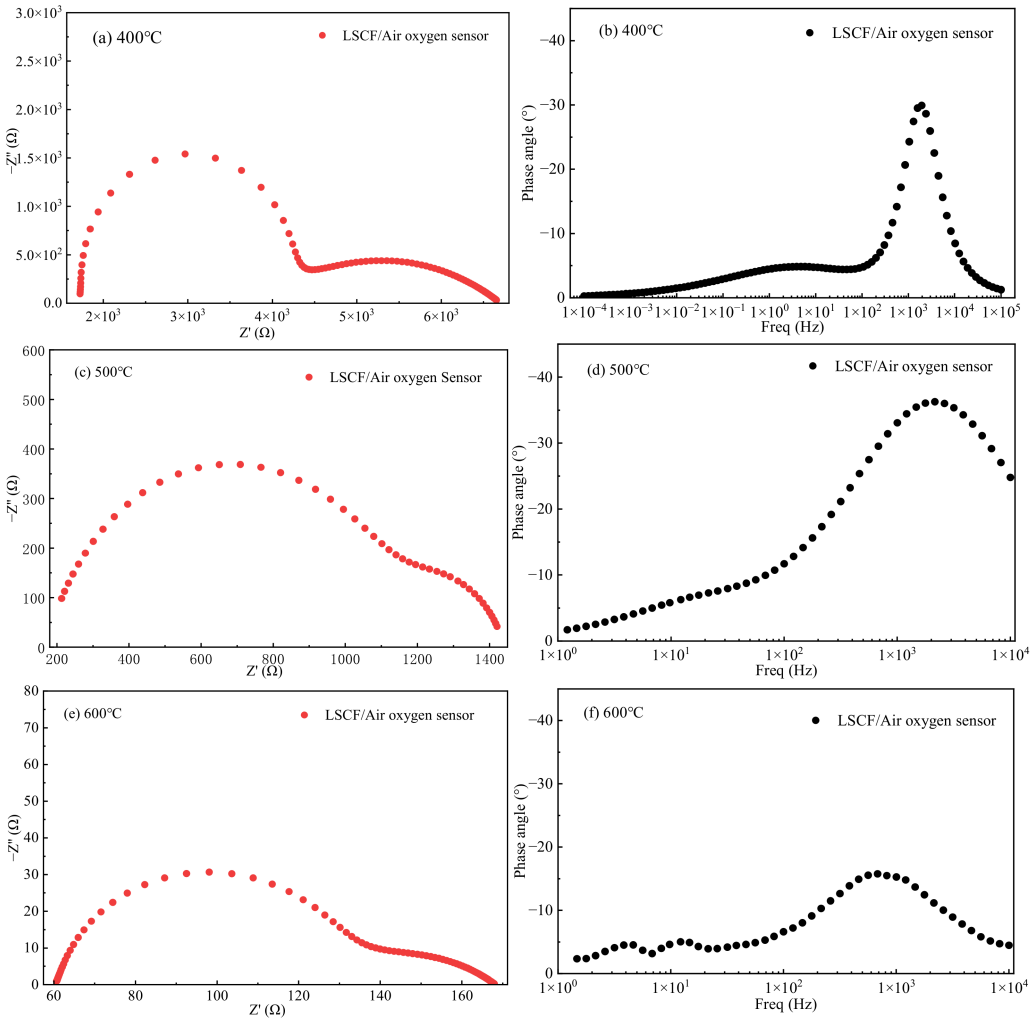


Figure 6. EIS results of the LSCF/Air oxygen sensor at different temperatures: Nyquist plots at (**a**) 400 °C, (**c**) 500 °C and (**e**) 600 °C; Bode phase-angle plots at (**b**) 400 °C, (**d**) 500 °C and (**f**) 600 °C.

The Nyquist impedance spectra of the Bi/Bi_2O_3 oxygen sensor are shown in Figure 7. Overall, as the temperature increases from 400 °C to 600 °C, the total polarization impedance at the electrode/YSZ interface decreases significantly, from the order of ~10^4 Ω to ~10^2 Ω.

At 400 °C, as shown in Figure 7a, the impedance spectrum shows a clear two-capacitive-arc feature. The high-frequency arc corresponds to the bulk ionic conduction response of the YSZ electrolyte, while the low-frequency arc reflects the oxygen ion transfer process at the Bi/Bi_2O_3–YSZ interface. At this temperature, the real-axis intercept of the low-frequency arc is approximately 2.6×10^4~3.1×10^4 Ω, and the peak value of the imaginary component reaches 2.5×10^4 Ω. This indicates that the interfacial oxygen ion exchange rate is extremely low at low temperature, and the ion injection barrier is high. When the temperature increases to 500 °C and 600 °C, as shown in Figure 7c,e, the impedance spectra evolve from two arcs into a single capacitive arc. This suggests that the relaxation times of the bulk and interfacial processes become closer, and the interfacial polarization impedance decreases greatly. It is worth noting that the significant shrinkage of the low-frequency arc means that interfacial ion exchange is no longer the rate-controlling step, and the interface tends to become electrochemically uniform.

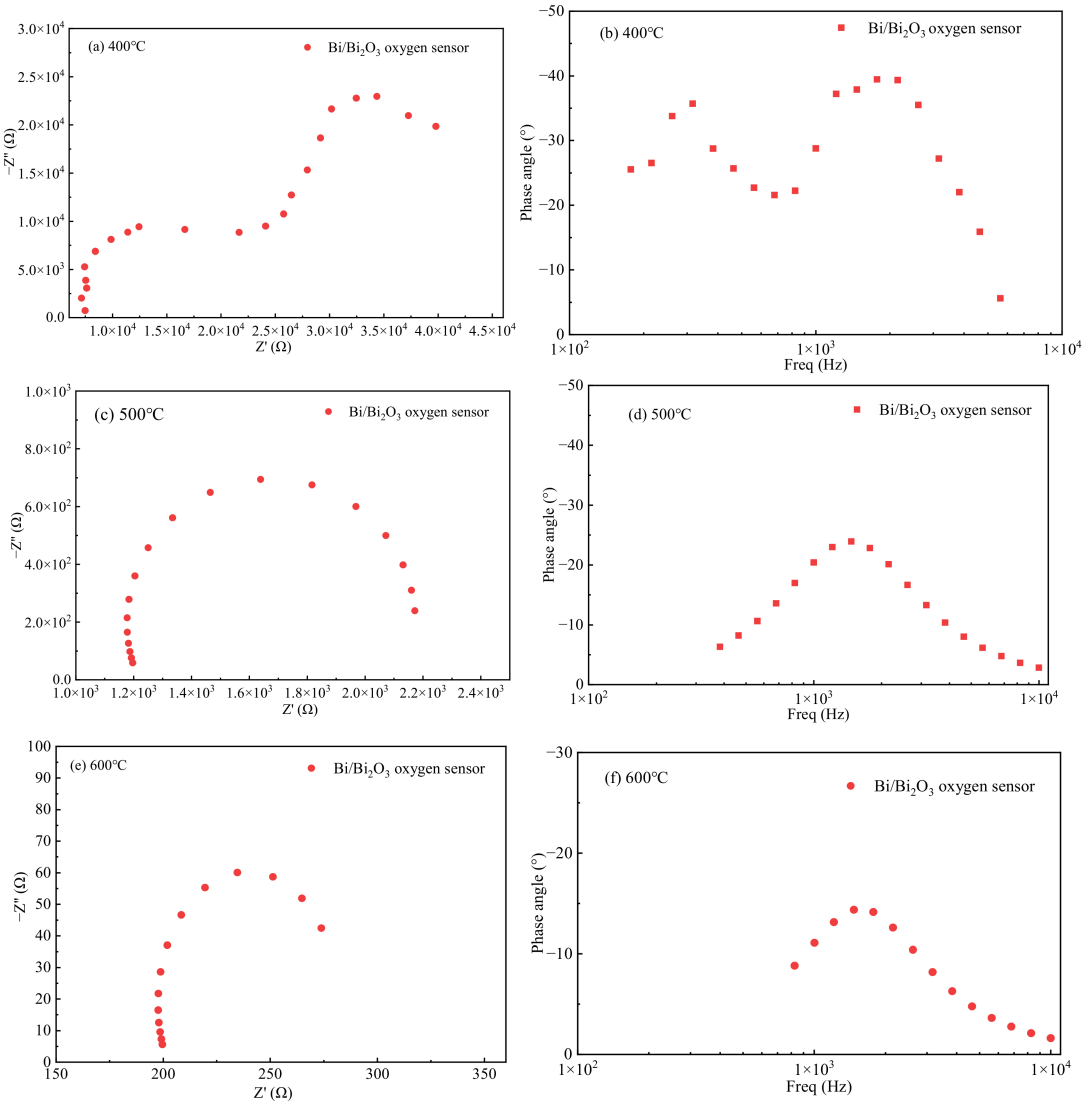


Figure 7. EIS results of the Bi/Bi_2O_3 oxygen sensor at different temperatures: Nyquist plots at (**a**) 400 °C, (**c**) 500 °C and (**e**) 600 °C; Bode phase-angle plots at (**b**) 400 °C, (**d**) 500 °C and (**f**) 600 °C.

The Bode phase-angle plots of the Bi/Bi_2O_3 system, shown in Figure 7b,d,f, indicate that its effective electrochemical response is mainly concentrated in the high-frequency region of 10^3~10^5 Hz. At 400 °C, the phase-angle curve shows a clear double-peak feature, suggesting that ideal and uniform electrochemical contact between liquid Bi and the 8YSZ solid electrolyte has not yet been formed. This is mainly because liquid Bi has relatively poor wettability at low temperature and is difficult to sufficiently penetrate into the microstructure of the YSZ surface. Therefore, significant interfacial contact impedance is generated. The local non-uniformity of the interface also gives rise to two distinguishable relaxation time constants in the high-frequency response. As the temperature increases to 500 °C, the two peaks gradually merge and transform toward a single peak. At 600 °C, the high-frequency response evolves into a relatively complete capacitive arc. This evolution indicates that increasing temperature significantly reduces the viscosity of liquid Bi and improves its wettability on the YSZ surface. As a result, the solid–liquid contact becomes tighter and more uniform, the interfacial contact impedance is greatly reduced, and the interfacial state tends to become electrochemically consistent.

To quantitatively analyze the interfacial polarization characteristics, the derived resistive parameters (R_1, R_2, R_3) are summarized in Table 1. It should be noted that while the

equivalent circuit incorporates constant phase elements, we specifically focus on reporting these resistive components, as they are the primary kinetically relevant variables utilized for the subsequent calculations of apparent ionic conductivity and activation energies.

Table 1. EIS fitting results of the resistive components for different electrode systems at various temperatures. Data are presented as mean ± standard deviation (N = 2).

Electrode	T/°C	R_1/Ω	R_2/Ω	R_3/Ω
LSCF/Air	400	1738.3 ± 18.0	4244.1 ± 750.7	1168.4 ± 23.4
LSCF/Air	500	176.9.3 ± 10.7	247.7 ± 56.1	999.1 ± 22.5
LSCF/Air	600	61.3 ± 1.5	64.2 ± 1.6	44.7 ± 2.9
Bi/Bi_2O_3	400	8272.5 ± 1604.4	514.0 ± 28.1	28,987.0 ± 3211.7
Bi/Bi_2O_3	500	1146.7 ± 43.2	881.0 ± 160.4	0
Bi/Bi_2O_3	600	195.2 ± 3.6	83.7 ± 10.6	0

To ensure the statistical significance and reliability of the reported results, two independent sensors (N = 2) were fabricated and tested for each electrode configuration (LSCF/Air and Bi/Bi_2O_3). Representative single-measurement EIS spectra are presented, but the parameter calculations were performed on both independent datasets. The fitting results and calculated conductivities are expressed as mean ± standard deviation (SD), as detailed in Tables 1 and 2. During the uncertainty propagation for apparent ionic conductivity, the variance in geometric dimensions (machined 8YSZ tubes) was verified to be negligible (tolerance < 0.02 mm); therefore, the uncertainty is primarily derived from the standard deviation of the measured impedance. As shown in the tables, the relative uncertainties at high temperatures (600 °C) are extremely small (<3%), demonstrating the excellent reproducibility of the sensor fabrication and measurement. Notably, the larger standard deviations observed for the Bi/Bi_2O_3 sensor at 400 °C (~19.4% for R_1) quantitatively reflect the physical randomness of the liquid–solid "point contact" interface caused by poor wettability at low temperatures. This further corroborates the kinetic limitations and instability of the Bi-based sensor in low-temperature LBE environments.

Table 2. Quantitative values and measurement uncertainties of apparent ionic conductivity (σ) and interfacial polarization area conductivity (G_P) at different temperatures. Data are presented as mean ± standard deviation (N = 2).

Electrode	T/°C	Apparent Ionic Conductivity σ (S/cm)	Interfacial Polarization Area Conductivity G_P (S^2/cm)
LSCF/Air	400	$(1.78 \pm 0.02) \times 10^{-5}$	$(7.24 \pm 0.97) \times 10^{-5}$
LSCF/Air	500	$(1.76 \pm 0.11) \times 10^{-4}$	$(3.11 \pm 0.08) \times 10^{-4}$
LSCF/Air	600	$(5.06 \pm 0.13) \times 10^{-4}$	$(3.56 \pm 0.04) \times 10^{-3}$
Bi/Bi_2O_3	400	$(3.82 \pm 0.74) \times 10^{-6}$	$(1.32 \pm 0.14) \times 10^{-5}$
Bi/Bi_2O_3	500	$(2.71 \pm 0.10) \times 10^{-5}$	$(4.48 \pm 0.82) \times 10^{-4}$
Bi/Bi_2O_3	600	$(1.59 \pm 0.03) \times 10^{-4}$	$(4.68 \pm 0.59) \times 10^{-3}$

Combined with the equivalent-circuit fitting data in Table 1, the interfacial polarization characteristics of the two reference electrode systems can be quantitatively compared. It should be noted that the physical origins of the low-frequency arcs are different in the two systems. For the LSCF/Air system, the low-frequency response mainly reflects the surface adsorption, dissociation, and diffusion processes of oxygen molecules. For the Bi/Bi_2O_3 system, it corresponds to oxygen ion injection across the liquid–solid interface. At 400 °C, the low-frequency polarization resistance of the LSCF system is 1.15×10^3 Ω, which is much lower than that of the Bi/Bi_2O_3 system, 3.13×10^4 Ω. This advantage is due to the mixed ionic–electronic conducting characteristics of LSCF. These characteristics

extend the electrochemically active region from the traditional triple-phase boundary to the whole electrode surface, giving good interfacial oxygen exchange kinetics even at low temperature. Therefore, the LSCF-based oxygen sensor is more suitable for low-temperature environments.

The bulk ionic conductivity (σ) of the solid electrolyte and the interfacial polarization area conductivity (G_p) were further analyzed for oxygen sensors with the two different electrode systems.

$$\sigma = \frac{1}{R_1 \bullet G_t} \tag{17}$$

σ is the ionic conductivity, with a unit of S/cm; R_1 is the ohmic resistance, with a unit of Ω. The bulk ionic conductivity of the 8YSZ solid electrolyte can be calculated accordingly. G_t is the bulk conduction geometric factor of the corresponding oxygen sensor, which is determined from the specific sensor geometry.

$$G_p = \frac{1}{R_p \bullet S_{in}} \tag{18}$$

G_p is the interfacial polarization area conductivity, with a unit of S/cm^2; R_p is the total polarization resistance, with a unit of Ω. S_{in} is the effective active area of the corresponding oxygen sensor, with a unit of cm^2.

Figure 8a shows that, at the same temperature, the apparent effective ionic conductivity calculated from the LSCF/Air system is significantly higher than that of the Bi/Bi_2O_3 system. It should be noted that this difference does not represent a real difference in the intrinsic bulk ionic conductivity of the 8YSZ electrolyte. Instead, it originates from the different physical contributions to the high-frequency intercept R_1 in the impedance spectra. In actual measurements, R_1 includes not only the intrinsic bulk resistance of the YSZ electrolyte, but also the ohmic contact resistance at the electrode/electrolyte interface connected in series. For the LSCF/Air system, this advantage is intrinsically linked to the mixed ionic–electronic conducting (MIEC) characteristics of LSCF. According to established solid-state electrochemistry literature [26], MIEC materials effectively extend the electrochemically active region from the traditional triple-phase boundary to the entire electrode surface. Although direct in-situ microstructural observation (e.g., cross-sectional SEM) was not performed here, our EIS results strongly align with the widely accepted phenomenological model (as schematically inferred in Figure 5) that LSCF establishes a highly effective solid–solid contact pathway with the YSZ inner wall upon high-temperature sintering. Therefore, the relatively low contact resistance allows the R_1 value to more closely reflect the bulk properties compared to the Bi-based system, although it remains an apparent measurement. Conversely, for the Bi/Bi_2O_3 system, it is fundamentally limited by the interfacial ion injection barrier. Based on well-documented liquid metal-ceramic wetting behaviors [27], the physical contact state between liquid Bi and the YSZ wall is largely governed by wettability mechanics. Therefore, it can be reasonably inferred that the remarkably large apparent impedance at 400 °C originates from the limited effective contact area and poor wettability of liquid Bi at low temperatures. In addition, the possible interfacial lattice mismatch between solid Bi/Bi_2O_3 and YSZ may further increase the interfacial barrier, resulting in a significant increase in contact resistance. In this case, R_1 is the sum of the bulk resistance and contact resistance. If R_1 is directly used to calculate the intrinsic conductivity, the obtained value will be seriously underestimated. Therefore, the difference in apparent effective ionic conductivity observed in Figure 8a essentially reflects the significant difference in ohmic contact quality between the two electrode systems and the YSZ electrolyte. This further demonstrates the applicability of the LSCF-based oxygen sensor at low temperature.

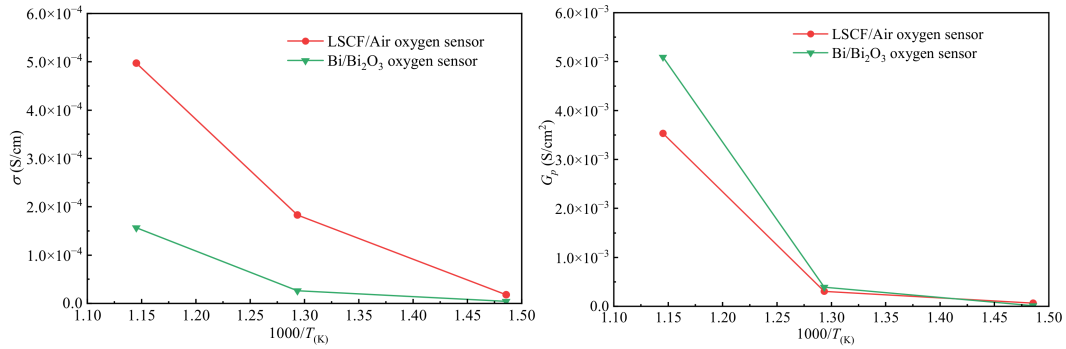


Figure 8. Comparison of solid-electrolyte ionic conductivity and interfacial polarization area conductivity in the oxygen sensor systems; (**a**) temperature dependence of apparent ionic conductivity, (**b**) temperature dependence of interfacial polarization area conductivity.

Figure 8b compares the temperature dependence of the polarization area conductivity of the two oxygen sensor systems. In the low-temperature region at 400 °C, the polarization area conductivities of the LSCF/Air and Bi/Bi_2O_3 systems are similar, and both remain at relatively low levels. However, the origins of their impedance are completely different. For the LSCF/Air system, the polarization impedance is limited by the slow adsorption/dissociation kinetics of oxygen molecules on the electrode surface at low temperature. For the Bi/Bi_2O_3 system, it is limited by the interfacial ion injection barrier caused by the limited solid–liquid contact area between liquid Bi and the YSZ wall. Therefore, the similar polarization resistance values of the two systems at low temperature are only a numerical coincidence observed in the experiment, rather than being caused by the same physical mechanism. As the temperature increases to 600 °C, the polarization area conductivities of both systems increase. However, the increase in the Bi/Bi_2O_3 system is more significant, and its polarization area conductivity becomes obviously higher than that of the LSCF/Air system at the same temperature. This change is attributed to the significant improvement in the wettability of liquid Bi on the YSZ surface in the temperature range of 500~600 °C. The liquid–solid contact state changes from sparse "point contact" at low temperature to continuous "area contact" at high temperature. The large increase in effective interfacial area directly leads to a rapid enhancement of the interfacial ion exchange rate. This further demonstrates the important influence of electrode/electrolyte interfacial polarization characteristics on the overall performance of the sensor.

The Arrhenius fitting lines of the ionic conduction behavior in the LSCF/Air and Bi/Bi_2O_3 oxygen sensors were further investigated.

$$\ln(\sigma \bullet T) = \ln(A) - \frac{E_a}{1000k_B} \bullet \left(\frac{1000}{T}\right) \quad (19)$$

where A is the pre-exponential factor representing the effective reaction/collision sites, and the unit is related to the region. k_B is the Boltzmann constant 8.617 × 10^{-5} eV/K, and E_a is the activation energy, expressed in eV. The slope of the fitted straight line directly reflects the activation energy E_a required to overcome the conduction barrier, while the intercept corresponds to the magnitude of the pre-exponential factor ln(A).

According to the Arrhenius plot of solid-electrolyte ionic conduction in Figure 9a, the bulk oxygen ion conduction activation energy E_a of the LSCF/Air oxygen sensor is approximately 0.92 eV, while that of the Bi/Bi_2O_3 system is approximately 0.97 eV. Both values fall within the typical range of 0.9–1.0 eV for oxygen vacancy hopping in bulk 8YSZ. This indicates that the evolution of high-frequency impedance in both sensors is mainly controlled by oxygen ion migration inside the YSZ lattice.

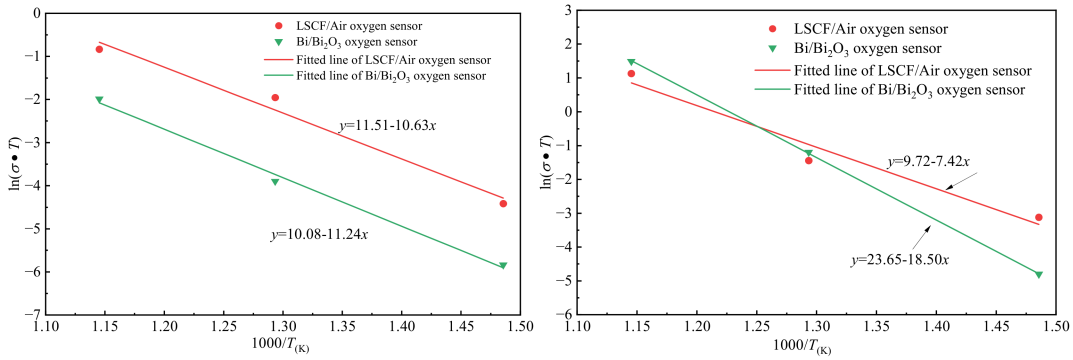


Figure 9. Arrhenius fitting plots for the LSCF/Air and Bi/Bi_2O_3 oxygen sensors; (**a**) ionic conduction in the solid electrolyte, (**b**) interfacial polarization conduction.

It is worth noting that, at the same temperature, the $\ln(\sigma \cdot T)$ values of the LSCF/Air system are systematically higher than those of the Bi/Bi_2O_3 system. This difference is not caused by a change in the intrinsic ionic conductivity of YSZ. Instead, it is caused by the non-negligible interfacial ohmic contact resistance connected in series with the high-frequency intercept R_1 in the Bi/Bi_2O_3 system. Therefore, the apparent conductivity calculated from the total resistance is underestimated. This inference is consistent with the equivalent-circuit analysis described above.

It must be explicitly emphasized that the remarkably higher apparent effective ionic conductivity derived from the LSCF/Air system does not represent a true enhancement in the intrinsic bulk transport properties of the 8YSZ electrolyte itself. As acknowledged above, the measured resistance (R_1) encompasses distinct interfacial contact contributions. Therefore, these apparent conductivity values primarily reflect the superior interfacial contact quality and significantly lower contact resistance of the LSCF electrode in low-temperature regimes, rather than an inherent superiority in electrolyte bulk transport.

Furthermore, according to the Arrhenius plot of interfacial polarization in Figure 9b, the interfacial polarization activation energy of the LSCF/Air system is approximately 0.64 eV, while the apparent polarization activation energy of the Bi/Bi_2O_3 system reaches 1.59 eV. The large difference between the two values reflects completely different interface-controlled mechanisms. In the LSCF system, the lower activation energy is attributed to the efficient interfacial oxygen exchange kinetics provided by its mixed ionic–electronic conducting characteristics. Therefore, its interfacial impedance has relatively low temperature sensitivity, which is beneficial for maintaining a stable sensor response over a wide medium- and low-temperature range.

In contrast, the high apparent activation energy of 1.59 eV for the Bi/Bi_2O_3 system does not represent the energy barrier of a single elementary reaction. Instead, it includes the combined contribution of a non-Arrhenius-type physical process associated with the threshold-like transition of liquid Bi wettability with temperature. This indicates that the interfacial polarization impedance of the Bi/Bi_2O_3 system is highly sensitive to temperature changes.

In addition, the intercepts $\ln(A)$ obtained from the Arrhenius fitting of the two systems are also significantly different. The value is 23.65 for the Bi/Bi_2O_3 system and 9.72 for the LSCF system. The intercept term reflects the combined effects of effective carrier concentration and hopping frequency. The larger intercept of the Bi/Bi_2O_3 system means that it has a higher upper limit of conductivity at high temperature. Combined with its high activation energy of 1.59 eV, this indicates that Bi/Bi_2O_3-based oxygen sensors are more suitable for high-temperature operating environments. In contrast, the lower activation energy and smaller intercept of the LSCF/Air sensor enable it to show better

ionic-conduction stability and stronger resistance to temperature disturbance in the low- to medium-temperature range.

4.3. Electrochemical Characterization of Irradiated 8YSZ

Oxygen ion irradiation experiments were conducted on 8YSZ, followed by electrochemical analysis of the irradiated samples. The oxygen ion irradiation was performed in the terminal chamber of the 320 kV low-energy heavy-ion comprehensive research platform. Polished 8YSZ ceramic samples were irradiated with 1.5 MeV O ions at room temperature, with an irradiation fluence of 8.0×10^{16} ions/cm^2, corresponding to a peak damage level of approximately 2 dpa. During irradiation, the vacuum in the sample chamber was maintained below 1×10^{-5} Pa. Three tests were conducted on both irradiated and non-irradiated samples, and the measurement errors for impedance and ionic conductivity are shown in Table 3.

Table 3. Standard Deviations in the Measurement of Impedance and Ionic Conductivity for Unirradiated and Irradiated Samples at Different Temperatures.

T/°C	Irradiation Conditions	Standard Deviation of Impedance Measurements/Ω	Standard Deviation in the Measurement of Ionic Conductivity/Ω
400	unirradiated	2.58×10^4	3.32×10^{-8}
400	2dpa	1.03×10^4	3.36×10^{-9}
500	unirradiated	6.40×10^3	1.04×10^{-7}
500	2dpa	5.77×10^3	5.29×10^{-8}
600	unirradiated	3.76×10^2	2.68×10^{-6}
600	2dpa	3.51×10^2	1.77×10^{-6}

As the test temperature increased from 400 °C to 600 °C, the radii of the Nyquist impedance arcs of both samples decreased significantly, and the total polarization impedance was greatly reduced, as shown in Figure 10a,c,e. This indicates that increasing temperature effectively lowers the activation barrier for oxygen ion migration and increases the hopping frequency of oxygen vacancies in the 8YSZ lattice. This fully reflects the typical thermally activated characteristic of ionic transport in solid electrolytes. At the same temperature, the 2 dpa oxygen ion-irradiated sample showed a higher impedance response than the unirradiated sample. In particular, at 400 °C, the impedance arc of the irradiated sample was much larger than that of the unirradiated sample. This indicates that the inhibition effect of irradiation damage on oxygen ion transport is more obvious at low temperature. With increasing temperature, the impedance difference between the two samples gradually decreased. However, even at 600 °C, the irradiated sample still showed slightly higher impedance. The Bode plots in Figure 10b,d,f further reveal the frequency-impedance magnitude response characteristics of the unirradiated and 2 dpa irradiated 8YSZ samples. With increasing frequency, the impedance magnitude of both samples gradually decreased, showing typical frequency dispersion behavior. At 400 °C, the irradiated sample showed a significantly higher impedance magnitude in the low-frequency region than the unirradiated sample. As the temperature increased to 500 °C and 600 °C, the overall impedance modulus of both samples decreased, and the curves gradually tended to overlap. However, the irradiated sample still maintained slightly higher impedance values in the low-frequency region, indicating that the irradiation-induced interfacial damaged layer had not fully recovered even at 600 °C.

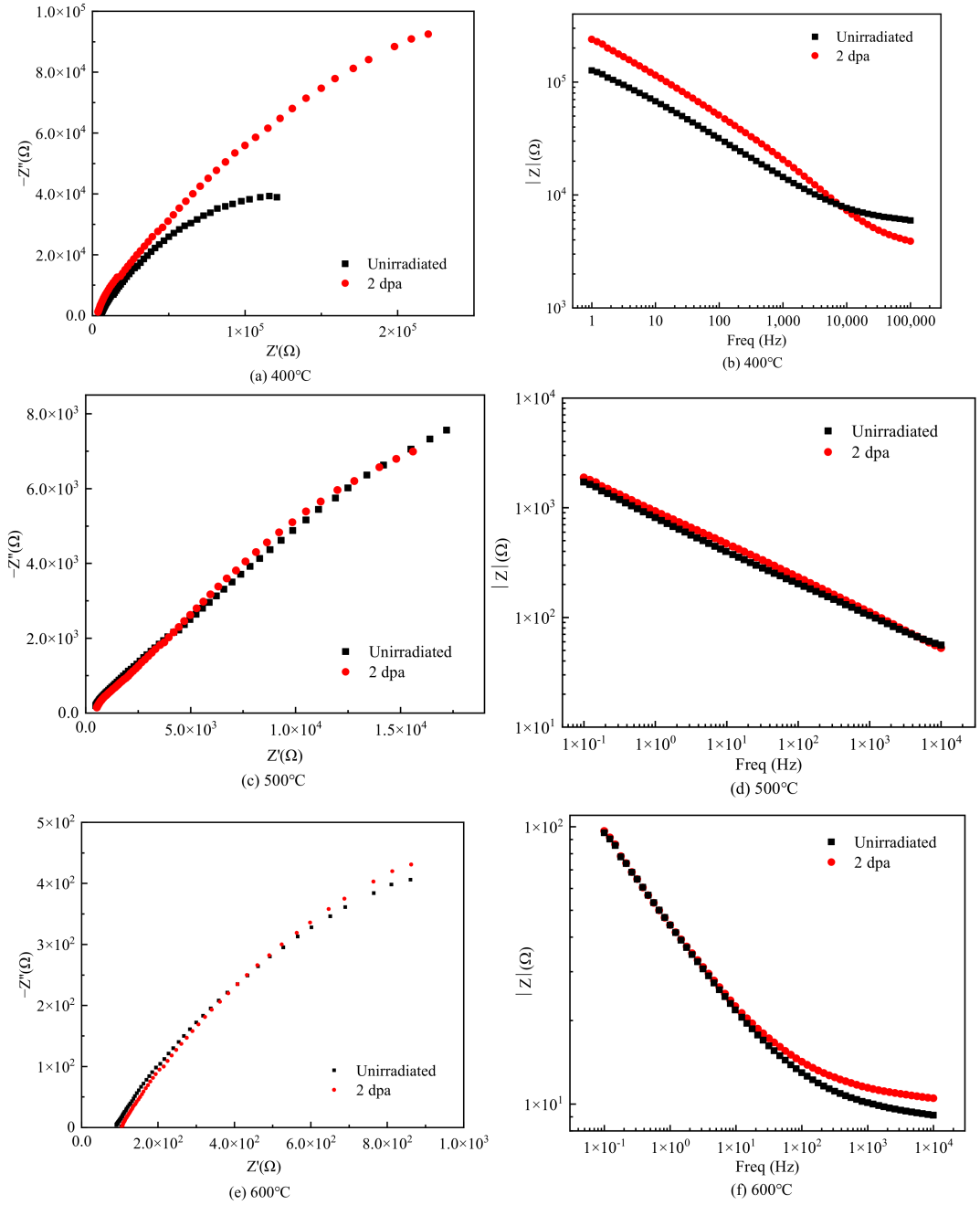


Figure 10. Electrochemical impedance spectra of unirradiated and 2 dpa oxygen ion-irradiated 8YSZ samples at different temperatures. Nyquist plots: (**a**) 400 °C, (**c**) 500 °C and (**e**) 600 °C. Frequency-impedance magnitude Bode plots: (**b**) 400 °C, (**d**) 500 °C and (**f**) 600 °C.

Figure 11 shows the temperature dependence of the apparent ionic resistance and oxygen ion conductivity of the unirradiated 8YSZ sample and the 2 dpa oxygen ion-irradiated 8YSZ sample. As shown in Figure 11a, the apparent ionic resistance of both samples decreased significantly as the test temperature increased from 400 °C to 600 °C. This indicates that increasing temperature can effectively promote thermally activated hopping of oxygen vacancies and reduce the resistance to ion migration. This also reflects the typical thermally activated characteristic of oxygen ion transport in 8YSZ. At the same temperature, the apparent ionic resistance of the 2 dpa irradiated sample was always higher than that of the unirradiated sample. Taking 400 °C as an example, the resistance of the irradiated sample was approximately 1.7 times that of the unirradiated sample. As the temperature increased, the difference between the two samples gradually decreased.

However, at 600 °C, the resistance of the irradiated sample was still approximately 1.5 times that of the unirradiated sample, and the difference remained distinguishable.

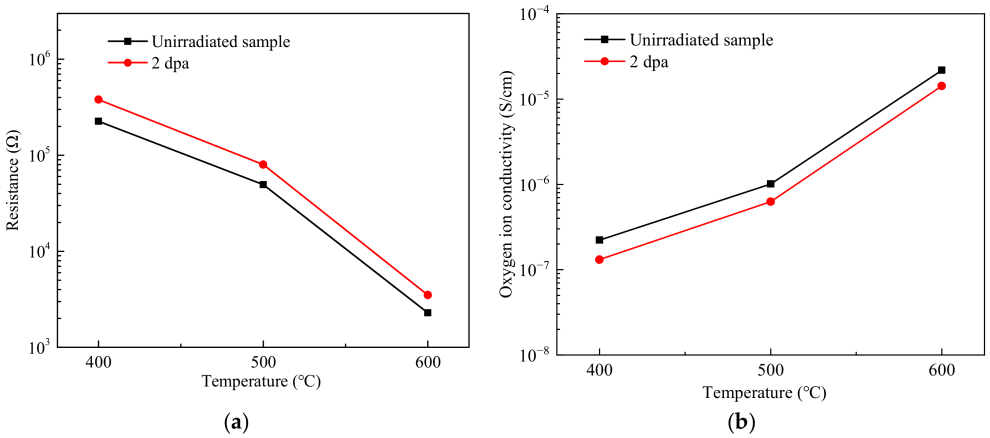


Figure 11. Temperature dependence of impedance and oxygen ion conductivity of unirradiated and 2 dpa O-ion-irradiated 8YSZ samples; (**a**) apparent ionic resistance, (**b**) apparent ionic conductivity.

Figure 11b shows the temperature dependence of oxygen ion conductivity. Its trend is opposite to that of resistance. The conductivity of both samples increased significantly with increasing temperature. This result further confirms the thermally activated nature of oxygen ion conduction in 8YSZ. Increasing temperature increases the probability that oxygen vacancies overcome the migration energy barrier, thereby increasing ionic mobility. In the whole temperature range of 400~600 °C, the oxygen ion conductivity of the irradiated sample was always lower than that of the unirradiated sample, which is consistent with the increased resistance shown in Figure 11a.

In summary, the EIS analysis shows that oxygen ion irradiation increased the apparent impedance and decreased the ionic conductivity of the tested 8YSZ sample/electrode system. However, the present EIS results alone cannot distinguish the individual contributions of these factors. Therefore, additional microstructural characterization and depth-resolved electrochemical measurements are required to identify the dominant mechanism.

5. Conclusions

This study systematically tested the output EMF of air reference oxygen sensors and metal/metal oxide reference oxygen sensors within the temperature ranges of 205~550 °C on the same experimental platform. By comparing the measured EMF values with the theoretical ones, the stability, measurement accuracy and response characteristics of LSCF/Air and Bi/Bi_2O_3 sensors within the corresponding temperature ranges were evaluated. Then, their electrochemical characteristics were analyzed to obtain the impedance properties and oxygen ion conductivity under corresponding temperature conditions. Additionally, 8YSZ was irradiated with oxygen ions, and the electrochemical properties of the irradiated samples were examined to determine the effects of irradiation on oxygen ion transport. The research results provide crucial benchmark data and selection criteria for the applicability of oxygen sensors in non-isothermal liquid LBE systems. The main research conclusions of this paper are as follows:

(1) The Bi/Bi_2O_3 oxygen sensor showed good Nernstian response in the temperature range of 350–550 °C. During stepwise cooling, obvious EMF relaxation appeared at the beginning of each cooling stage, which was related to the non-steady-state temperature change and the delayed interfacial equilibrium process. When the temperature was lower than 350 °C, the output signal deviated obviously from the theoretical value. At 295 °C, the EMF was about 35 mV lower than the theoretical value, and

the relative deviation reached −39.95%, indicating that the Bi/Bi_2O_3 sensor was not suitable for low-temperature oxygen measurement.

(2) The LSCF/Air oxygen sensor showed better stability and accuracy in a wider temperature range. In the range of 205~550 °C, the output EMF agreed well with the theoretical values, and the maximum relative error was only −1.28%. Compared with the Bi/Bi_2O_3 sensor, the LSCF/Air sensor had less obvious relaxation behavior and better low-temperature applicability. Although signal relaxation appeared near 200 °C, the overall sensor response remained acceptable after sufficient holding time.

(3) EIS results showed that the two sensors had different interfacial polarization mechanisms. The LSCF/Air sensor showed lower polarization resistance at low temperature. In contrast, the Bi/Bi_2O_3 sensor showed large interfacial resistance at low temperature. Oxygen ion irradiation increased the impedance and decreased the ionic conductivity of 8YSZ.

Author Contributions: Conceptualization, Z.M. and R.L.; methodology, Y.W.; software, Y.W. and Z.X.; validation, Z.M., Y.W. and Z.X.; formal analysis, R.L.; investigation, Z.M.; resources, R.L.; data curation, Z.M.; writing—original draft preparation, Z.M.; writing—review and editing, Z.M.; visualization, R.L.; supervision, F.N.; project administration, F.N.; funding acquisition, F.N. and R.L. All authors have read and agreed to the published version of the manuscript.

Funding: This research is supported by the National Natural Science Foundation of China (12027813) and the Fundamental Research Funds for the Central Universities (2025MS058).

Data Availability Statement: The data analyzed in this study can be obtained from the corresponding author upon reasonable request.

Conflicts of Interest: The authors declare no conflict of interest.

References

1. Holbert, K.E. A Review of Maritime Nuclear Reactor Systems. *J. Nucl. Eng.* **2025**, *6*, 5. [CrossRef]
2. Gianfelici, S.; Grasso, G. Research on the safety of heavy-liquid-metal-cooled reactors. *EPJ Nucl. Sci. Technol.* **2025**, *11*, 29. [CrossRef]
3. Giot, M.; Cirillo, R.; D'Haeseleer, W.; Moons, F.; Van Goethem, G. The European Nuclear Education Network: 20 years of service to the nuclear fission community. *Nucl. Eng. Des.* **2024**, *419*, 112974. [CrossRef]
4. Panizo, S.; Alfonso, C.; Jiménez-Carrascosa, A.; García-Herranz, N.; Bécares, V.; Romojaro, P.; Álvarez-Velarde, F.; Cabellos, O.; Cuesta-Matesanz, A.; Fiorito, L.; et al. Sensitivity and uncertainty analyses for advanced nuclear systems (ALFRED, ASTRID, ESFR and MYRRHA). *Prog. Nucl. Energy* **2024**, *172*, 105207. [CrossRef]
5. Chubarov, M.; Zakharov, M.; Bogdanova, E.; Smirnov, A.; Ouen, D.; Tikhomirov, G. Development of a test task for coupled neutronic and thermal-hydraulic analysis of LFR fuel cell. *Nucl. Eng. Technol.* **2025**, *57*, 103763. [CrossRef]
6. Askhadullin, R.S.; Martynov, P.N.; Rachkov, V.I.; Legkikh, A.Y.; Storozhenko, A.N.; Ulyanov, V.V.; Gulevskiy, V.A. Monitoring and control of the oxygen content in heavy liquid-metal coolants for anticorrosion protection of steels. *High Temp.* **2016**, *54*, 564–572. [CrossRef]
7. Sadovnichiy, R.P.; Skomorohov, A.N.; Legkikh, A.Y.E.; Askhadullin, R.S.E.; Lotov, V.S. The Steam-Hydrogen-Based Method for Reproducing Oxygen Thermodynamic Activity in Lead-Containing Alloys to Verify Oxygen Activity Sensors. *Izv. Vyss. Uchebnykh Zaved. Yad. Energ.* **2022**, *2022*, 89–101. [CrossRef]
8. Courouau, J.L.; Deloffre, P.; Adriano, R. Oxygen control in lead-bismuth eutectic: First validation of electrochemical oxygen sensors in static conditions. *J. Phys. IV* **2002**, *12*, 141–153. [CrossRef]
9. Courouau, J.; Sellier, S.; Chabert, C.; Pignoly, L. Electrochemical oxygen sensor for on-line measurement in liquid lead alloy systems at relatively low temperature. *Afinidad* **2005**, *62*, 464–468.
10. Schroer, C.; Konys, J.; Verdaguer, A.; Abellà, J.; Gessi, A.; Kobzova, A.; Babayan, S.; Courouau, J. Design and testing of electrochemical oxygen sensors for service in liquid lead alloys. *J. Nucl. Mater.* **2011**, *415*, 338–347. [CrossRef]
11. Lim, J.; Manfredi, G.; Mariën, A.; Van den Bosch, J. Performance of potentiometric oxygen sensors with LSM-GDC composite electrode in liquid LBE at low temperatures. *Sens. Actuators B Chem.* **2013**, *188*, 1048–1054. [CrossRef]
12. Bassini, S.; Antonelli, A.; Di Piazza, I.; Tarantino, M. Oxygen sensors for Heavy Liquid Metal coolants: Calibration and assessment of the minimum reading temperature. *J. Nucl. Mater.* **2017**, *486*, 197–205. [CrossRef]

13. Wu, X.; Ma, J.; Jiang, Y.; Fu, B.; Hang, W.; Zhang, J.; Li, N. Instrumentation of YSZ oxygen sensor calibration in liquid lead-bismuth eutectic. *Rev. Sci. Instrum.* **2005**, *76*, 075104.
14. Kurata, Y.; Abe, Y.; Futakawa, M.; Oigawa, H. Characterization and re-activation of oxygen sensors for use in liquid lead-bismuth. *J. Nucl. Mater.* **2010**, *398*, 165–171. [CrossRef]
15. Zhu, C.; Qu, G.; Zhai, L.; Zhou, M.; Qiu, X.; Gao, Y.; Long, Z.; Yang, J. Heavy-ion-irradiation effect of yttrium-stabilized-zirconia coatings on microstructure and lead-bismuth corrosion. *Radiat. Phys. Chem.* **2025**, *227*, 112370. [CrossRef]
16. Ghyngazov, S.; Boltueva, V. Effect of ion treatment on the structure and properties of ceramic materials (review). *Ceram. Int.* **2023**, *49*, 37061–37071. [CrossRef]
17. Ghyngazov, S.; Boltueva, V.; O'Connell, J.H.; Vershinina, T.N.; Kirilkin, N.S.; Rymzhanov, R.A.; Skuratov, V.A.; Surzhikov, P. Swift heavy ion induced phase transformations in partially stabilized ZrO_2. *Radiat. Phys. Chem.* **2022**, *192*, 109917. [CrossRef]
18. Pu, G.; Zou, J.; Lin, L.; Zhang, K.; Liu, B.; Ma, F.; Wang, Q.; Li, Q. Effects of He ion irradiation on the microstructures and mechanical properties of t′ phase yttria-stabilized zirconia ceramics. *J. Alloys Compd.* **2019**, *771*, 777–783. [CrossRef]
19. Alin, M.; Kozlovskiy, A.L.; Zdorovets, M.V.; Uglov, V.V. Study of the mechanisms of the t-ZrO_2 → c-ZrO_2 type polymorphic transformations in ceramics as a result of irradiation with heavy Xe^{22+} ions. *Solid State Sci.* **2022**, *123*, 106791. [CrossRef]
20. NEA. *Handbook on Lead-Bismuth Eutectic Alloy and Lead Properties, Materials Compatibility, Thermal-Hydraulics and Technologies—2015 Edition*; OECD Publishing: Paris, France, 2015.
21. Kishimoto, A.; Wada, A.; Michimoto, T.; Furukawa, T.; Aoto, K.; Oishi, T. Solubility and Activity of Oxygen in Pb–Bi Melts. *Mater. Trans.* **2006**, *47*, 122–128. [CrossRef]
22. Ganesan, R.; Gnanasekaran, T.; Srinivasa, R.S. Diffusivity, activity and solubility of oxygen in liquid lead and lead–bismuth eutectic alloy by electrochemical methods. *J. Nucl. Mater.* **2006**, *349*, 133–149. [CrossRef]
23. Manfredi, G.; Lim, J.; Rosseel, K.; Van den Bosch, J.; Doneux, T.; Buess-Herman, C.; Aerts, A. Comparison of solid metal–metal oxide reference electrodes for potentiometric oxygen sensors in liquid lead–bismuth eutectic operating at low temperature ranges. *Sens. Actuators B Chem.* **2015**, *214*, 20–28. [CrossRef]
24. Liang, R.; Li, H.; Zhu, H.; Wu, H.; Lyu, H.; Hao, Z.; Liu, Y.; Liu, F.; Niu, F. Performance of multiple-type reference electrode oxygen sensors in LBE. *Ann. Nucl. Energy* **2026**, *230*, 112129. [CrossRef]
25. Ghetta, V.; Fouletier, J.; Henault, M.; Le Moulec, A. Control and monitoring of oxygen content in molten metals. Application to lead and lead-bismuth melts. *J. Phys. IV* **2002**, *12*, 123–140. [CrossRef]
26. Adler, S.B. Factors governing oxygen reduction in solid oxide fuel cell cathodes. *Chem. Rev.* **2004**, *104*, 4791–4844. [CrossRef]
27. Eustathopoulos, N.; Chatain, D.; Nikopoulos, A.K. Wetting and interfacial chemistry in liquid metal–ceramic systems. *J. Mater. Sci.* **1991**, *26*, 2661–2678.

Disclaimer/Publisher's Note: The statements, opinions and data contained in all publications are solely those of the individual author(s) and contributor(s) and not of MDPI and/or the editor(s). MDPI and/or the editor(s) disclaim responsibility for any injury to people or property resulting from any ideas, methods, instructions or products referred to in the content.